

Thermodynamic Analysis of Solid Oxide Fuel Cell Based Combined Cooling, Heating, and Power System Integrated with Solar-Assisted Electrolytic Cell

GAO Yuefen, YAO Wenqi, WANG Jiangjiang^{*}, CUI Zhiheng

Hebei Key Laboratory of Low Carbon and High Efficiency Power Generation Technology, North China Electric Power University, Baoding 071003, China

© Science Press, Institute of Engineering Thermophysics, CAS and Springer-Verlag GmbH Germany, part of Springer Nature 2022

Abstract: Syngas fuel such as hydrogen and carbon monoxide generated by solar energy is a promising method to use solar energy and overcome its fluctuation effectively. This study proposes a combined cooling, heating, and power system using the reversible solid oxide fuel cell assisted by solar energy to produce solar fuel and then supply energy products for users during the period without solar radiation. The system runs a solar-assisted solid oxide electrolysis cell mode and a solid oxide fuel cell mode. The thermodynamic models are constructed, and the energetic and exergetic performances are analyzed. Under the design work conditions, the SOEC mode's overall system energy and exergy efficiencies are 19.0% and 20.5%, respectively. The electrical, energy and exergy efficiencies in the SOFC mode are 51.4%, 71.3%, and 45.2%, respectively. The solid oxide fuel cell accounts for 60.0% of total exergy destruction, caused by the electrochemical reactions' thermodynamic irreversibilities. The increase of operating temperature of solid oxide fuel cell from 800°C to 1050°C rises the exergy and energy efficiencies by 11.3% and 12.3%, respectively. Its pressure from 0.2 to 0.7 MPa improves electrical efficiency by 13.8% while decreasing energy and exergy efficiencies by 5.2% and 6.0%, respectively.

Keywords: solid oxide electrolysis cell (SOEC), solid oxide fuel cell (SOFC), solar energy, combined cooling, heating, and power (CCHP), exergy analysis

1. Introduction

The conventional energy utilization method relying on fossil fuels is changing and restructuring with the proposal of carbon neutrality [1]. The high proportion integration of renewable energies on improving fuel utilization efficiency is a promising way to mitigate the growing energy and environmental issues.

Combined cooling, heating, and power (CCHP) system were widely regarded as energy-saving methods to satisfy the multiple demands of electricity, cooling, and heating. The hybridization of solar energy in fuel

CCHP systems has attracted more attention [2] because of solar energy's inexhaustibility and mature technologies [3]. Besides, the introduction of solar energy compensates for the fact that most CCHP systems utilize only fossil fuels such as natural gas and improves system's flexibility, reliability, and cleanliness [2]. But solar energy is often uncertain and intermittent, making it challenging to match supply and demand between the CCHP systems and users. Transforming solar energy to fuel at the time of abundant solar irradiation and utilizing fuel to produce energy products for users at the time without solar irradiation is one of alternative methods to

Nomenclature

Abs	absorber
ARS	absorption refrigeration system
C	condenser
CCHP	combined cooling heating and power
COP	coefficient of performance
E	evaporator
HG	high pressure generation
HX	heat exchanger
HTX	high temperature heat exchanger
LHV	low heat value
LG	low pressure generation
LTX	low temperature heat exchanger
MRS	methane reforming reaction
ORC	organic Rankine cycle
PV	photovoltaic
PTSC	parabolic trough solar collectors
RGibbs	gibbs reactor
RStoic	stoichiometric reactor
R_U	reactant utilization ratio
RWGS	reverse water gas shift
SOCs	solid oxide cells
SOFC	solid oxide fuel cell
SOEC	solid oxide electrolysis cell
WGS	water gas shift

Symbols

A	area/m ²
Ex	the specific exergy/kW
ex	the exergy ratio/kJ·kmol ⁻¹
e	electrode porosity
E_n	Nernst voltage/V
E_{an}	activation energy of anode/kJ·mol ⁻¹
E_{ca}	activation energy of cathode/kJ·mol ⁻¹
F	Faraday constant/K·kmol ⁻¹
H	enthalpy/kJ
h	the specific enthalpy/kJ·kmol ⁻¹
G	electrical energy demand/kJ·kmol ⁻¹
J	current/A
j	current density/A·m ⁻²
k	the pre-exponential factor/A·m ⁻²
M	the mass flow rate/kg·h ⁻¹
m	the mole flow rate/kmol·h ⁻¹

N	solid oxide fuel cell quantity
P	power/kW
p	pressure/MPa
R	universal gas constant, 8.314 kJ/(kmol·K)
r	mean radius of electrode pore/m
T	temperature/°C
t	thickness/m
U	fuel utilization of fuel cell
V	voltage/V
W	the electrical power/kW

Greek letters

α	conversion rate/%
δ	molar fraction/%
η	efficiency/%
Λ	irreversibility loss
ω	concentration

Subscripts

act	the activation over potential
avg	average
an	the anode of fuel cell
ca	the cathode of fuel cell
comp	compressor
cell	fuel cell
conc	the concentration over potential
che	chemical
chilled	chilled water
dhw	domestic hot water
des	the destruction of exergy
ele	the electrical power
en	the specific energy
ex	the specific exergy
heat	heat output
in	input
inv	dc-ac inverter
net	the net power output
OP	operating
ohmic	the ohmic over potential
out	output
phy	physical exergy
tur	turbine
0	the state of ambient environment

improve high proportional rate of solar energy [4], in which solid oxide cells (SOCs) can fulfil these functions to utilize solar energy in CCHP systems [5]. SOCs consist of solid oxide electrolysis cell (SOEC) and solid

oxide fuel cell (SOFC) modes [6]. The SOEC mode can be combined with renewable energy and electrolysis of water (H₂O) or carbon dioxide (CO₂) into carbon monoxide (CO) and hydrogen (H₂). In contrast, the

SOFC mode can use methane (CH_4) or syngas of CO and H_2 as a fuel for power generation [7].

The electrolysis in the SOEC is a feasible solution to use the surplus electricity from renewable energy power generation, such as solar photovoltaic (PV) panels, which relieve the difficulty of a larger number of electricity storage [8]. Furthermore, the co-electrolysis of CO_2 and H_2O occurring in the SOEC effectively uses CO_2 through carbon capture [9]. Then, the specific chemical devices can convert syngas (CO and H_2) produced by electrolysis into fuels such as natural gas or methanol [10]. SOEC has a high electrolysis rate and energy conversion efficiency, and it is also flexibly adjusted according to demand. A diesel engine integrated SOEC system is proposed, and the electric efficiency of this system can reach 85.17% after waste heat recovery and utilization [11]. A novel combined heating and power generation system combining RSOFC and solar energy was proposed in Ref. [12], and the electrolytic efficiency of SOEC and the efficiency of the solar-assisted system are 85.1% and 20%, respectively. Making the co-electrolysis of CO_2 and H_2O in SOEC is considered one of the most feasible and energy-efficient techniques for converting CO_2 and H_2O into fuel [13]. Qi et al. [14] proposed a management strategy and thermodynamic analysis method for high-temperature co-electrolysis of $\text{H}_2\text{O}/\text{CO}_2$, which indicated that a high $\text{H}_2\text{O}/\text{CO}_2$ ratio should avoid carbon deposition at low temperature. The syngas produced by co-electrolysis of CO_2 and H_2O will be converted to CH_4 or adding methanation reactors in the system [15]. Producing syngas from CO_2 and H_2O at high temperatures was introduced in Ref. [16], which also provided the electrolytic step. Xi et al. [17] successfully developed an $\text{H}_2\text{O}/\text{CO}_2$ co-electrolysis model using flat-tube SOEC and studied its electrochemical performance and durability. The results show that nickel loss and aggregation are essential causes of cathode degradation. A SOEC reactor containing ten flat cells with a total effective area of 640 cm^2 was proposed to test the performance of co-electrolysis of CO_2 and H_2O , which achieved quantitative regulation of CO and H_2 products [18]. The electrolysis products were directly sent into the methanation reactor containing Ni catalyst and the 40 vol%–50 vol% CH_4 fuel was produced, which initially confirmed the feasibility and reliability of co-electrolysis of H_2O and CO_2 to produce hydrocarbon fuel [19]. However, adding methanation reactors or other reactants increases not only the system complexity of but also the investment cost. The SOFC with high running temperature allows to the combination of internal fuel reformation, using a variety of fuel options. Thus, the syngas electrolyzed by the SOEC can be used as fuels directly to drive SOFC [20].

SOFC is a clean and energy-efficient conversion

technology that converts a fuel's chemical energy directly into electrical energy and works at high temperatures [21], which is less susceptible to fuel composition changes and more suitable for syngas from SOEC as fuel [22]. Carbon-containing gases like CH_4 or CO have higher energy densities than pure H_2 . The high power generation efficiency of SOFC can be as the core component of CCHP systems, and the high-temperature exhaust gases from SOFC are easily integrated with gas turbine cycles [23]. A novel CCHP system that combines a SOFC subsystem, an Organic Rankine Cycle (ORC) subsystem, and an absorption chiller with a CO_2 capture subsystem was proposed in Ref. [24], which showed the exergy efficiency reached 59.96%.

However, in most of the current studies, the materials of RSOFC are the focus of analysis, and the SOEC mode provides H_2 for SOFC. Besides, renewable energy is rarely combined with fuel cells. In this study, H_2O and CO_2 co-electrolysis is used to provide syngas (including CO and H_2), which ensures the safety of the equipment and meets SOFC requirements for syngas fuels. At the same time, the proposed system adds the excess solar energy to generate electricity through the photovoltaic effect to provide electricity for SOEC, which can reduce the purchase of electricity from the power grid, and the cost is saved. The electrolysis process requires a large amount of electricity to produce fuel gas. This paper introduces a solar collector and PV to preheat and electrolysis H_2O and CO_2 , respectively, to reduce electricity consumption. Meanwhile, the thermodynamics and performance analyses of SOFC based on a solar-assisted CCHP system integrated with SOEC are studied. Finally, analyzing the variable parameters of the system, the key factors affecting system efficiency are determined, and then the optimal operation mode of the system is determined. New contributions to this work consist of the following:

- (1) A new hybrid CCHP system is proposed to integrate with a solar-assisted SOEC and a SOFC to improve energy conversion, storage, and utilization efficiency significantly. An energy-cascade method combines a turbine and an absorption chiller to recycle and utilize the high-temperature waste heat from SOFC.

- (2) The thermodynamic models of the hybrid CCHP system are constructed, and the thermodynamic performances in both solar-assisted SOEC and SOFC modes are analyzed. By verifying the subsystem, the energy and exergy performances of the system under design working conditions are obtained. Furthermore, the exergy Sankey diagram of exergy flow is given.

- (3) The system energy outputs and thermodynamic performances in variable working conditions were analyzed. The influences of main parameters are studied, including the ratio of H_2 to CO mole flow rate, the

running temperature and pressure of SOFC, the fuel utilization, and the percentage of H_2O to CO_2 mole flow rate.

The remaining structure of this paper is as follows: Section 2 demonstrates the energy flows of the proposed CCHP system and constructs the thermodynamic models; Section 3 describes the exergy analysis and performance indicators of solar-assisted SOEC and SOFC; Section 4 shows the results and discussion; Section 5 summarizes the significant conclusions.

2. Energy Flows and Modeling

2.1 System description

Fig. 1 demonstrates the proposed solar-assisted SOEC and CCHP system's energy flows. The system consists of a solar-assisted SOEC subsystem, SOFC subsystem and heat recovery subsystem. The solar-assisted SOEC subsystem converts CO_2 , H_2O and a small amount of H_2 by electrolysis to syngas fuel (CO and H_2) for the SOFC subsystem during higher solar radiation. When there is no solar radiation or at night, the SOFC uses syngas from SOEC as fuel to produce power for users. Finally, the heat-recovery subsystem uses the high-temperature waste gas from SOFC to deliver cooling and heating for consumers.

The specific principle of the working process can be summarized as follows: CO_2 , H_2O , and a small amount of H_2 (point 1) from the storage tank are preheated to high-temperature gases (point 2) by absorbing the solar heat collected by parabolic trough solar collectors (PTSC). In this SOEC subsystem, in the RGibbs reactor, H_2 and CO_2 are transformed into CO and H_2O (point 3) by the reverse water gas shift (RWGS) reaction. Besides, the RStoic reactor in ASPEN PLUS is used to simulate the co-electrolysis occurring in SOEC, the co-electrolysis of CO_2 and H_2O promotes the production of CO and H_2 (point 5), and a small amount of CH_4 reacts with H_2O through methane reforming reaction (MSR) to encourage the production of CO and H_2 further. Furthermore, the solar PV provides power for the co-electrolysis of CO_2 and H_2O to produce syngas fuel (point 6). After that, the syngas are compressed by a compressor and released heat to the operating temperature of the SOFC before entering the anode, which combines with compressed and preheated cathode air (point 8) and produces an electrochemical reaction in the RGibbs reactor in ASPEN PLUS.

The high-temperature and high-pressure exhaust gas (point 11) are produced by the combustion of underutilized cathode and anode gases in the afterburner, which allows more power to be generated by the turbine.

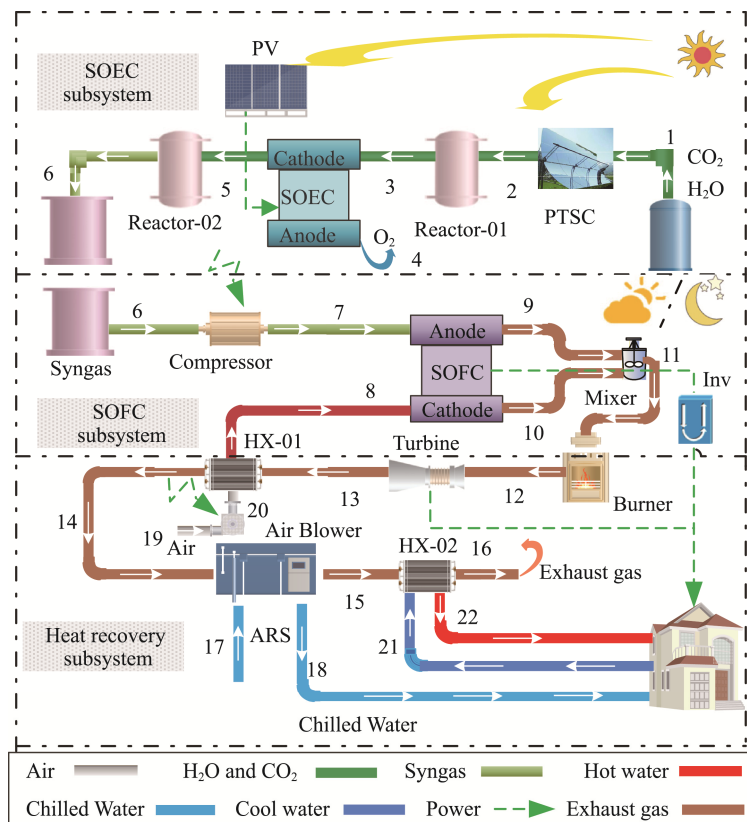


Fig. 1 Energy flows of the solar-assisted SOEC and CCHP system. (PTSC-parabolic trough solar collector; HX-heat exchanger; ARS-absorption refrigeration system; Inv-inverter)

The waste heat of the exhaust gas (point 13) generated by the turbine enters the HX-01 heat exchanger and preheats the air (point 19), and then the preheated air enters the anode. In addition, the double-effect Libr-H₂O absorption unit is driven by the remaining exhaust gas (point 14) to generate the cooling or heating. Besides, the exhaust gas (point 15) from the absorption refrigeration system (ARS) can heat tap water in HX-02 to produce domestic hot water. In the end, the remaining exhaust gas (point 16) is released into the atmosphere.

2.2 Thermodynamic modeling

The proposed CCHP system was established and simulated by Aspen Plus V11, and the electrochemical model and evaluation criteria of the proposed system were simulated in MATLAB and Fortran, respectively.

2.2.1 Models' assumptions

Some assumptions are considered in the model constructions and simulations:

- (1) The current and voltage of the system are evenly distributed in each cell unit.
- (2) The operating temperature and operating pressure under the two operating modes are the same, and the outlet gas temperature is consistent with the operating temperature.
- (3) The air composition is 79% N₂ and 21% O₂.
- (4) The chemical reaction is carried out under steady-state conditions and meets the thermodynamic equilibrium.
- (5) The internal pressure and temperature distribution of SOFC and SOEC are uniform and equal.
- (6) The afterburner combusts the underutilized fuel gas of SOFC completely.
- (7) The ambient pressure and temperature in this paper are 101.325 kPa and 25°C, respectively.

2.2.2 Solar modules

In this paper, solar modules include PV and PTSC, the total solar energy input to the system, P_{solar} , can be calculated as:

$$P_{\text{solar}} = P_{\text{solar,PV}} + P_{\text{solar,PTSC}} \quad (1)$$

where $P_{\text{solar,PV}}$ and $P_{\text{solar,PTSC}}$ represent the solar energy received by the PV and PTSC, respectively, which can be defined as:

$$P_{\text{solar,PV}} = I_{\text{solar}} \cdot A_{\text{PV}} \quad (2)$$

$$P_{\text{solar,PTSC}} = \text{DNI} \cdot A_{\text{PTSC}} \quad (3)$$

where I_{solar} and DNI denote the full solar radiation and direct normal irradiation, respectively; A_{PV} and A_{PTSC} indicate the installed area of PV and PTSC, respectively.

The amount of electricity that PV needs to provide ($P_{\text{ele,PV}}$) and the heat from PTSC (Q_{PTSC}) can be defined as:

$$P_{\text{ele,PV}} = \eta_{\text{PV}} P_{\text{solar,PV}} = V_{\text{SOEC}} J_{\text{SOEC}} \quad (4)$$

$$Q_{\text{PTSC}} = \eta_{\text{PTSC}} P_{\text{solar,PTSC}} = m_1 (h_2 - h_1) \quad (5)$$

where V_{SOEC} and J_{SOEC} represent the output potential and current of SOEC, respectively. η_{PV} and η_{PTSC} indicate the conversion efficiency of PV and PTSC, respectively, which can be calculated as:

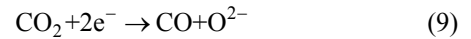
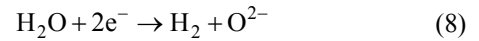
$$\eta_{\text{PV}} = \frac{P_{\text{max,PV}}}{P_{\text{solar,PV}}} \quad (6)$$

$$\eta_{\text{PTSC}} = \eta_{\text{OP}} \left(1 - \frac{\sigma T_{\text{PTSC}}^4}{\text{DNI} \cdot C_{\text{R}}} \right) \quad (7)$$

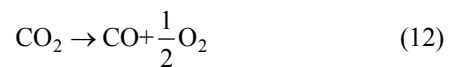
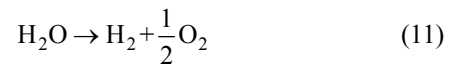
where $P_{\text{max,PV}}$ denotes the maximum power output of PV, which depends on the characteristics of PV panels and can be found in Ref. [12]. η_{OP} and T_{PTSC} are the solar energy optical efficiency and the temperature of the PTSC, respectively. C_{R} indicates the concentrating ratio, and σ is $5.67 \times 10^{-8} \text{ W}/(\text{m}^2 \cdot \text{K}^4)$, the specific characteristics and model of PTSC can be referred to Ref. [25].

2.2.3 Solar-assisted SOEC system

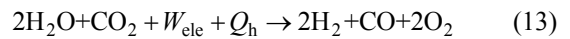
The SOEC efficiently performs the co-electrolysis of H₂O and CO₂. In this paper, the RStoic reactor in ASPEN PLUS is used to simulate the co-electrolysis occurring in SOEC, and the co-electrolysis of CO₂ and H₂O promotes the production of CO and H₂. Besides, the energy needed for SOEC is provided by solar energy. The electrolytic reactions of CO₂ and H₂O at the SOEC cathode and the anodic oxidation reactions of oxygen ions are as follows:



The complete reactions are as follows:

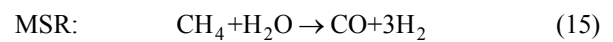
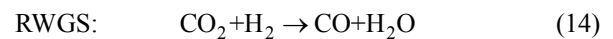


The co-electrolysis of CO₂ and H₂O is expressed as:



where W_{ele} and Q_{h} respectively represent the electric energy and heat energy required by the electrolysis reaction.

Simultaneously, the conversion of CO₂ and CH₄ are accompanied by two equilibrium reactions which are the RWGS and MSR reaction as:



The total energy demand (ΔH) of the solar-assisted SOEC is determined as:

$$\Delta H = T \Delta S + \Delta G \quad (16)$$

where $T\Delta S$ and ΔG are the thermal energy demand and electrical energy demand of co-electrolysis, respectively.

The electrochemical model determines the electrical energy involved in the SOEC operation:

$$\dot{W}_{\text{SOEC}} = V_{\text{SOEC}} J_{\text{SOEC}} \quad (17)$$

where J_{SOEC} is the current provided by the solar PV; \dot{W}_{SOEC} denotes the electrical energy involved in the SOEC mode, and V_{SOEC} represents the output potential of SOEC as follows:

$$V_{\text{SOEC}} = E_n + \eta_{\text{conc,an}}^{\text{SOEC}} + \eta_{\text{conc,ca}}^{\text{SOEC}} + \eta_{\text{act,an}} + \eta_{\text{act,ca}} + \eta_{\text{ohmic}} \quad (18)$$

where E represents the Nernst potential; $\eta_{\text{conc,an}}^{\text{SOEC}}$, $\eta_{\text{conc,ca}}^{\text{SOEC}}$, $\eta_{\text{act,an}}$, $\eta_{\text{act,ca}}$ and η_{ohmic} are concentration overpotential of the anode, concentration overpotential of the cathode, activation overpotential of the anode, activation overpotential of the cathode, and the ohmic overpotential of the electrolyte, respectively. These overpotential models can be found in Ref. [26].

The current density of SOEC, j_{SOEC} , is defined as:

$$j_{\text{SOEC}} = \frac{J_{\text{SOEC}}}{NA_{\text{cell}}} = \frac{nF \times R_U \times n_{\text{H}_2\text{O,eq}}}{NA_{\text{cell}}} \quad (19)$$

$$n_{\text{H}_2\text{O,eq}} = n_{\text{fuel,SOEC}} (\delta_{\text{H}_2\text{O}} + \delta_{\text{CO}_2}) \quad (20)$$

$$R_U = \frac{M_{\text{out}} - M_{\text{in}}}{M_{\text{in}}} = \frac{J_{\text{SOEC}}}{nFM_{\text{in}}} \quad (21)$$

where N and A_{cell} are respectively the quantity and the active cell area of SOEC; n represents the transferred electronic amount ($n=2$) per mole H_2O ; R_U is the reactant utilization ratio of electrolytic cell; $n_{\text{H}_2\text{O,eq}}$ is the mole equivalent flow rate of H_2O ; $n_{\text{fuel,SOEC}}$, $\delta_{\text{H}_2\text{O}}$ and δ_{CO_2} are the fuel needed by SOEC and the molar fraction of H_2O and CO_2 , respectively; M_{in} and M_{out} are the inlet and outlet flows of reactants, respectively. Furthermore, the detailed R_U can be found in Ref. [27].

The Nernst potential of SOEC can be determined by:

$$E_n = 1.253 - 2.4516 \times 10^{-4} T_{\text{SOEC}} + \frac{RT}{2F} \ln \left[\frac{P_{\text{H}_2}^0 (P_{\text{O}_2}^0)^{1/2}}{P_{\text{H}_2\text{O}}^0} \right] \quad (22)$$

where R denotes the universal gas constant; T_{SOEC} is the operating temperature of SOEC; F represents the Faraday constant. Besides, $P_{\text{H}_2\text{O}}^0$, $P_{\text{O}_2}^0$ and $P_{\text{H}_2}^0$ are the partial pressures of H_2O , O_2 , and H_2 of SOEC, respectively.

The heat generated by SOEC overpotential can be represented as:

$$A = 2F (\eta_{\text{conc,an}}^{\text{SOEC}} + \eta_{\text{conc,ca}}^{\text{SOEC}} + \eta_{\text{act,an}} + \eta_{\text{act,ca}} + \eta_{\text{ohmic}}) \quad (23)$$

When $A \geq T\Delta S$, the heat generated by SOEC can meet the H_2O and CO_2 co-electrolysis reaction's heat demand,

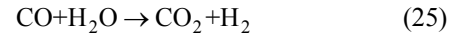
thus $Q_{\text{h,SOEC}}=0$. Inversely, if $\sigma < T\Delta S$, the additional heat energy is required as:

$$Q_{\text{h,SOEC}} = [T\Delta S - A] n_{\text{H}_2\text{O,eq}} \quad (24)$$

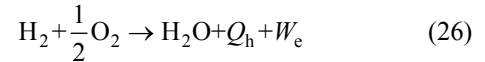
2.2.4 SOFC system

SOFC uses the RGibbs reactor in ASPEN PLUS to simulate the water-gas shift (WGS) reaction and electrochemical reaction, where the fuel is syngas produced by SOEC. The two reactions are expressed as:

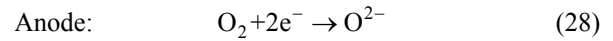
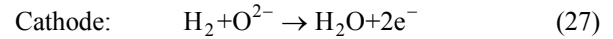
WGS:



Electrochemical reaction:



The specific cathode and anode reactions are as follows:



The generated electrical power by SOFC is estimated as:

$$\dot{W}_{\text{SOFC}} = V_{\text{SOFC}} J_{\text{SOFC}} \quad (29)$$

where V_{SOFC} is the output voltage of SOFC, which can be expressed as:

$$V_{\text{SOFC}} = E_n - \eta_{\text{conc,an}}^{\text{SOFC}} - \eta_{\text{conc,ca}}^{\text{SOFC}} - \eta_{\text{act,an}} - \eta_{\text{act,ca}} - \eta_{\text{ohmic}} \quad (30)$$

where the concentration overpotential ($\eta_{\text{conc,an}}^{\text{SOFC}}$ and $\eta_{\text{conc,ca}}^{\text{SOFC}}$) modeling equations can be found in Ref. [28].

The current density of SOFC, j_{SOFC} , is defined by [29]:

$$j_{\text{SOFC}} = \frac{J_{\text{SOFC}}}{NA_{\text{cell}}} = \frac{nR_{\text{U,fuel}} F \times n_{\text{H}_2\text{,eq}}}{NA_{\text{cell}}} \quad (31)$$

$$n_{\text{H}_2\text{,eq}} = n_{\text{fuel,SOFC}} (\delta_{\text{H}_2} + \delta_{\text{CO}} + 4\delta_{\text{CH}_4}) \quad (32)$$

$$R_{\text{U,fuel}} = \frac{n_{\text{H}_2\text{,consumed}}}{n_{\text{H}_2\text{,eq}}} \quad (33)$$

$$n_{\text{O}_2\text{,consumed}} = \frac{n_{\text{H}_2\text{,consumed}}}{2} \quad (34)$$

where $R_{\text{U,fuel}}$ represents the fuel utilization rate of SOFC; $n_{\text{H}_2\text{,consumed}}$ and $n_{\text{O}_2\text{,consumed}}$ are the H_2 and O_2 molar flow rate consumed by SOFC, respectively; $n_{\text{H}_2\text{,eq}}$ is the H_2 mole equivalent flow rate; $n_{\text{fuel,SOFC}}$ is the flow rate of fuel to the SOFC, and δ_i denote the molar fraction of the fuel components i .

The electricity generation of SOFC (W_{ele}) and its net power output ($W_{\text{ele,net}}$) are respectively expressed as:

$$W_{\text{ele}} = \eta_{\text{DC/AC}} \dot{W}_{\text{SOFC}} \quad (35)$$

$$W_{\text{ele,net}} = W_{\text{ele}} - W_{\text{comp}} \quad (36)$$

where $\eta_{\text{DC/AC}}$ represents the inverter efficiency; W_{comp} is the total electric power consumption of compressors.

2.2.5 Gas turbine

The model Compr simulates the GT and compressor in ASPEN PLUS, and the following equation can calculate the energy balance equation:

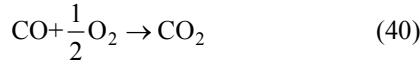
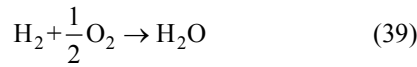
$$W_{\text{tur}} = m_{12} (h_{12} - h_{13}) \cdot \eta_{\text{tur}} \quad (37)$$

$$W_{\text{comp}} = m_6 (h_6 - h_7) \cdot \eta_{\text{comp}} \quad (38)$$

where W_{tur} and W_{comp} indicate the electricity generated by the GT and the electricity consumed by the compressor, respectively; η_{tur} and η_{comp} represent the efficiency of the GT and compressor, respectively.

2.2.6 Afterburner

An Aspen Plus reactor module Rstoic is selected to simulate the combustion reaction of SOFC outlet gas as:



2.2.7 Double LiBr-H₂O ARS

The double-effect LiBr-H₂O ARS uses lithium bromide as the working fluid, and its coefficient of performance (COP) is higher than that of single-effect ARS. The model Heater simulates the ARS in ASPEN PLUS, and the mass, solute, and energy balance equations of the chiller can be expressed to:

$$\sum m_{\text{input}} = \sum m_{\text{output}} \quad (41)$$

$$\sum m_{\text{input}} \omega_{\text{input}} = \sum m_{\text{output}} \omega_{\text{output}} \quad (42)$$

$$\sum m_{i,\text{input}} h_{i,\text{input}} = \sum m_{j,\text{output}} h_{j,\text{output}} \quad (43)$$

where ω represents the solution concentration.

Some basic assumptions and models about the refrigeration process were given in our teamwork [30], and the details of the absorption cooling/heating are shown in Fig. 2.

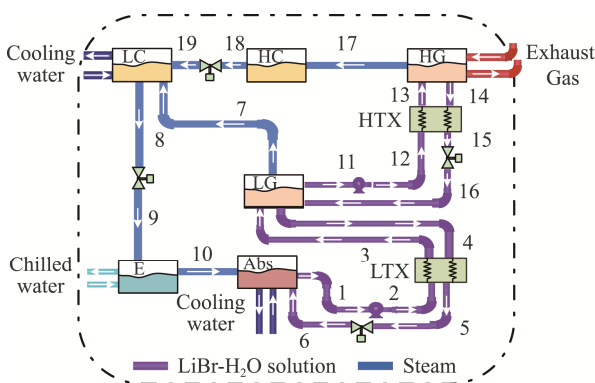


Fig. 2 Schematic diagram of ARS. (Abs-absorber; E-evaporator; HC-high pressure condenser; HG-high pressure generation; HTX-high temperature heat exchanger; LC-low pressure condenser; LG-low pressure generation; LTX-low temperature heat exchanger)

2.2.8 Heat exchanger

In this paper, the preheating of cathode air and the preparation of domestic hot water need HX-01 and HX-02 respectively. The model HeatX simulates the HX in ASPEN PLUS, and the energy balance equation can be expressed as:

$$\text{HX-01: } m_{20} (h_8 - h_{20}) = m_{13} (h_{13} - h_{14}) \quad (44)$$

$$\text{HX-02: } m_{21} (h_{22} - h_{21}) = m_{15} (h_{15} - h_{16}) \quad (45)$$

3. Exergy Analysis and Performance Indicators

3.1 Exergy modeling

According to the second law of thermodynamics, all irreversible processes must overcome resistance. Exergy analysis plays a significant role in determining the source of exergy destruction, good workflow, and system performance optimization. Therefore, the application and implementation of exergy analysis is beneficial to evaluating the performance of the proposed system.

It is assumed that the environment, H₂O, and CO₂ are stable, and the heat dissipation loss of equipment and pipeline to the environment in electrolysis is ignored. The exergy of the matter is composed of physical exergy and chemical exergy, and the exergy of a substance (Ex) can be calculated as:

$$Ex = Ex_{\text{che}} + Ex_{\text{phy}} \quad (46)$$

where Ex_{che} represents chemical exergy; Ex_{phy} is physical exergy, and they are respectively determined as [31]:

$$Ex_{\text{phy}} = \sum_i (H_i - H_0) - T_0 (S_i - S_0) \quad (47)$$

$$Ex_{\text{che}} = RT_0 \sum x_i \ln(x_i) + \sum x_i Ex_{\text{che},i} \quad (48)$$

where the subscript 0 represents the reference environment condition; H denotes enthalpy; S is entropy; x_i represents the molar composition of the specified gas, and the specific standard exergy of gas $Ex_{\text{che},i}$ can be found in Ref. [31]. The exergy of solar radiation Ex_{solar} can be calculated as:

$$Ex_{\text{solar}} = \left[1 + \frac{1}{3} \left(\frac{T_0}{T_s} \right)^4 - \frac{4}{3} \frac{T_0}{T_s} \right] P_{\text{solar}} \quad (49)$$

where P_{solar} is total solar radiation power; T_0 is the environment temperature, and T_s represents the sun temperature (6000 K) [2].

The exergy generated after converting of solar energy can be calculated as follows:

$$Ex_{\text{solar,cs}} = P_{\text{e,pv}} + \left(1 - \frac{T_0}{T_{\text{SOEC}}} \right) Q_{\text{PTSC}} \quad (50)$$

where $Ex_{\text{solar,cs}}$ represents the exergy generated after that solar energy is converted into heat and electricity; T_{SOEC} denotes the operating temperature of SOEC.

The heat exergy is defined as:

$$Ex_Q = \left(1 - \frac{T_0}{T}\right) Q_h \quad (51)$$

The exergy destruction $Ex_{des,i}$, the exergy destruction fraction $Ex_{des,i}^{ratio}$, and the exergy efficiency $\eta_{ex,i}$ can be respectively defined as:

$$Ex_{des,i} = \sum Ex_{in,i} - \sum Ex_{out,i} \quad (52)$$

$$Ex_{des,i}^{ratio} = \frac{Ex_{des,i}}{\sum_{i=1}^n Ex_{des,i}} \quad (53)$$

$$\eta_{ex,i} = \frac{Ex_{out,i}}{Ex_{in,i}} = 1 - \frac{Ex_{des,i}}{Ex_{in,i}} \quad (54)$$

3.2 Performance indicators

3.2.1 Evaluation of SOEC

The energy efficiency of SOEC (η_{en}^{SOEC}) and solar-assisted SOEC ($\eta_{en,solar-assisted}^{SOEC}$) are determined by:

$$\eta_{en}^{SOEC} = \frac{LHV_{H_2} M_{H_2,out} + LHV_{CO} M_{CO,out}}{\dot{W}_{SOEC} + Q_{heat,SOEC} + Q_{PTSC} + Q_{SOEC,reaction}} \quad (55)$$

$$\eta_{en,solar-assisted}^{SOEC} = \frac{LHV_{H_2} M_{H_2,out} + LHV_{CO} M_{CO,out}}{P_{solar}} \quad (56)$$

where LHV represents the lower heating value; $M_{H_2,out}$ and $M_{CO,out}$ are the outlet flow rates of H_2 and CO , respectively; $Q_{SOEC,reaction}$ is the energy demand of both RWGS and MSR reactions.

Their exergy efficiencies can be, respectively, defined as:

$$\eta_{ex}^{SOEC} = \frac{Ex_{H_2} M_{H_2,out} + Ex_{CO} M_{CO,out}}{Ex_{solar,cs}} \quad (57)$$

$$\eta_{ex,solar-assisted}^{SOEC} = \frac{Ex_{H_2} M_{H_2,out} + Ex_{CO} M_{CO,out}}{Ex_{solar}} \quad (58)$$

where Ex_{H_2} and Ex_{CO} are the exergy content of H_2 and CO_2 .

3.2.2 Evaluation of SOFC

The gross energy efficiency ($\eta_{en,CCHP}$), electrical efficiency (η_{ele}), and exergy efficiency ($\eta_{ex,CCHP}$) of the CCHP system based on SOFC can be, respectively, calculated as:

$$\eta_{en,CCHP} = \frac{W_{ele,net} + W_{tur} + Q_{cooling} + Q_{dhw}}{LHV_{H_2} M_{H_2,in} + LHV_{CO} M_{CO,in}} \quad (59)$$

$$\eta_{ele} = \frac{W_{ele,net} + W_{tur}}{LHV_{H_2} M_{H_2,in} + LHV_{CO} M_{CO,in}} \quad (60)$$

$$\eta_{ex,CCHP} = \frac{W_{ele,net} + W_{tur} + \left(\frac{T_0}{T_{chilled}} - 1\right) Q_{cooling}}{Ex_{H_2} M_{H_2,in} + Ex_{CO} M_{CO,in}} + \frac{\left(1 - \frac{T_0}{T_{dhw}}\right) Q_{dhw}}{Ex_{H_2} M_{H_2,in} + Ex_{CO} M_{CO,in}} \quad (61)$$

where $Q_{cooling}$ and Q_{dhw} are the cooling output and heat output of domestic hot water of the CCHP system, respectively; T_{dhw} is the temperature of domestic hot water; $T_{chilled}$ denotes the temperature of chilled water; $M_{H_2,in}$ and $M_{CO,in}$ are the inlet flow rates of H_2 and CO , respectively.

4. Results and Discussions

4.1 Model validation

Under the same conditions (CO_2 and H_2O are input at standard temperature and pressure, and the concentration ratio of CO_2 to H_2O is 2:1), the validation results of the SOEC model in this paper and Cinti G. et al. [27] are expressed in Table 1. The relative errors of the ratio of H_2/CO , current density, and output potential are 4.17%, 0.12% and 4.19%, respectively. Besides, the syngas with the percentage of H_2/CO greater than 2 is more suitable for the SOFC subsystem, which proves the validity of the proposed SOEC model.

Table 1 Validation results of the SOEC model

Parameter	Our model	Ref. [27]	Error/%
Outlet gas composition CO_2 /%	15.3	16.1	4.91
Outlet gas composition CO /%	14.7	15.5	4.98
Outlet gas composition H_2 /%	35.8	35.7	0.27
Ratio of H_2/CO	2.4	2.3	4.17
Current density/ $A \cdot m^{-2}$	4925.6	4931.7	0.12
Output potential/V	1.37	1.43	4.19

Table 2 represents the comparisons between our simulation results and the results in Refs. [32] and [33] under the same conditions. The relative errors of voltage, electric power, and electric efficiency are less than 5%, proving the electrochemical model established is suitable and further confirms the reliability of SOFC modeling.

Table 3 demonstrates the comparison results between this paper and Ref. [34] after stimulation by ASPEN PLUS. A double-effect absorption chiller's COP is the ratio of heat absorbed by the evaporator and HG. The maximum error can be calculated from the simulation results to be -2.30%, which indicates the accuracy of the ARS model.

Table 2 Our simulation results and the established results in Refs. [32] and [33]

SOFC	Ref. [32]	Our model	Error/%	Ref. [33]	Our model	Error/%
Voltage/V	0.70	0.73	3.98	0.66	0.68	1.97
Current density/A·m ⁻²	1780	1785	0.28	1887	1886	0.05
CH ₄ conversion/%	25.90	25.70	0.76	16.90	17.50	3.54
SOFC exhaust temperature/°C	834	835	0.12	829.70	830.50	0.09
Afterburner temperature/°C	1012	1014	0.19	994.10	995.40	0.13
Electric power/kW	119.70	124.80	4.26	120.10	122.30	1.91
Gross AC efficiency/%	52	54.10	4.04	42.53	43.36	1.95

Table 3 The relative error of the ARS

Parameter	Ref. [34]	Simulation	Deviation/%
Q_E /kW	354.37	346.4	-2.30
Q_{HG} /kW	255.43	254.5	-0.36
COP	1.387	1.36	-2.16

4.2 Performances under design conditions

The design parameters under the design work conditions are obtained and selected by our variable parameter simulations and analysis. The design objective is to improve system efficiency combined with the actual operating conditions. The design parameters of the overall system are determined in Table 4. The detailed SOFC parameters, including voltage losses, and geometric and physical parameters, are illustrated in Table 5.

Table 4 Design parameters under design working conditions

Parameter	Value
Steam/CO ₂ ratio, S/C	2
Operating temperature and pressure of SOEC, T_{SOEC}/P_{SOEC} , °C/MPa	800/0.2
DC/AC efficiency, $\eta_{DC/AC}$	0.92
Full solar irradiation, $I_{solar}/W \cdot m^{-2}$	1000
Reactant utilization of SOEC, R_U	0.45
Solar energy optical efficiency, $\eta_{op}/\%$	65
Fuel cell active area, A_{cell}/m^2	46.1 (1152 cells)
Inlet H ₂ O and CO ₂ temperature of SOEC, $T_{inlet}/°C$	329
Mechanical and isentropic efficiency of the turbine	0.9/0.8
Power required to supply SOEC/kW	104.5
Direct normal irradiation, DNI/ $W \cdot m^{-2}$	800
Mechanical and isentropic efficiency of the turbine	0.9/0.8
Fuel conversion rate of SOFC, $R_{U,fuel}$	0.85
Current density, $j/A \cdot m^{-2}$	1497
Mechanical efficiency of compressor	0.85
Operating temperature and pressure of SOFC, T_{SOFC}/P_{SOFC} , °C/MPa	800/0.2

4.2.1 Energy performances

It can be seen from Table 6 that the energy and exergy efficiencies of SOEC reach 86.9% and 66.8%, respectively. But when considering solar energy input in the SOEC subsystem, they are reduced to 19.0% and 20.5%, respectively. Although the high-temperature co-electrolysis technology is mature and has high efficiency and flexibility characteristics, the utilization rate of solar energy is relatively low.

Furthermore, Table 7 represents the simulation results of the SOFC system under design conditions. The energy and exergy efficiencies of the CCHP system based on SOFC are 71.3% and 45.2%, respectively, in which the electrical efficiency of SOFC is 51.4%. The pie chart of power ratios for all outputs is shown in Fig. 3. Among the products, electric energy accounted for 61.6% of the total energy output, which significantly affects the system's performance. This is because fuel cells are more efficient, allowing syngas to be harnessed in SOFC, and the unused, thin fuel then turns turbines to generate electricity. Finally, the remaining high-temperature exhaust gas provides 20.7 kW cooling and 2.9 kW domestic hot water.

4.2.2 Exergy performances

Fig. 4 demonstrates the Sankey diagrams of the exergy flow in the SOEC and SOFC modes under the design parameters. In the solar-assisted SOEC system, the 582.2 kW exergy of solar energy is fed to the PV and PTSC, which is converted into 127.4 kW of heating and electricity. Then, the energy is mixed with CO₂, H₂O and H₂ to react in SOEC to generate 119.7 kW of syngas, in which 33.2% of total exergy was destructed. The thermodynamic properties of the streams of the proposed system are shown in Table 8.

In the SOFC mode, the 119.7 kW syngas is compressed by compressor to 126 kW and participates in the electrochemical reaction of SOFC, which generates 37.3% of exhaust gas and 37.4% of electricity accompanied by 25.3% of exergy destruction. The residual flue gas and a small amount of unreacted syngas enter the after-combustion chamber to participate in the

Table 5 Design parameters of SOFC model [32]

Item	Parameter	Value
Geometry	Active area, S/m^2	46.08 (1152 cells)
	Anode thickness, t_{an}/cm	0.05
	Cathode thickness t_{ca}/cm	0.005
	Electrolyte thickness, t_{E}/cm	0.002
	Interconnection thickness, t_{int}/cm	0.0085
	Interconnection width, w_{int}/cm	0.9
Material properties	Anode resistivity, $\rho_{\text{an}}/\Omega\cdot\text{cm}$	$2.97\times10^{-3}\exp(-1391/T_{\text{op}})$
	Cathode resistivity, $\rho_{\text{ca}}/\Omega\cdot\text{cm}$	$8.11\times10^{-3}\exp(600/T_{\text{op}})$
	Electrolyte resistivity, $\rho_{\text{E}}/\Omega\cdot\text{cm}$	$2.94\times10^{-3}\exp(10\,350/T_{\text{op}})$
	Interconnection resistivity, $\rho_{\text{int}}/\Omega\cdot\text{cm}$	2.5
Ohmic loss	A/B	0.804/0.13
Activation loss	Pre-exponential factor $k_{\text{an}}/k_{\text{ca}}/\text{A}\cdot\text{m}^{-2}$	$5.5\times10^8/7\times10^8$
	Activation energy $E_{\text{an}}/E_{\text{ca}}$, kJ/kmol	100 000/117 000
	Electrode pore radius, r/m	5×10^{-7}
Concentration loss	Electrode porosity, $e/\text{tortuosity}$, x	0.5/5.9

Table 6 Simulation results of solar-assisted SOEC system at design conditions

Parameter	Item	Energy	Exergy
Input	Solar energy/kW	626.9	585.2
	Solar energy after conversion/kW	136.2	127.4
	H ₂ :10%, CO ₂ :30%, H ₂ O:60%	23.5	27.5
	Electrolysis power/kW	54.7	—
Output	Syngas, kW (H ₂ :35.81%, CO:14.66%, CO ₂ :15.34%, CH ₄ :0.01%, H ₂ O:34.18%)	118.4	119.8
Performance	SOEC efficiency/%	86.9	66.8
	Solar-assisted system efficiency/%	19.0	20.5

Table 7 Simulation results of SOFC system at design conditions

Parameter	Item	Energy	Exergy
Input	Syngas/kW (H ₂ :35.81%, CO:14.66%, CO ₂ :15.34%, CH ₄ :0.01% H ₂ O:34.18%)	118.4	119.8
Power consumption	Compressor-01/kW	7.3	—
Output	SOFC power, DC/AC/kW	52.0/47.8	52.0/47.8
	Turbine/kW	8.8	8.8
	Cooling/kW	20.7	1.1
	Domestic hot water/kW	2.9	0.2
	Net Electricity/kW	53.0	53.0
Performance	Electrical efficiency/%	51.4	—
	System efficiency/%	71.3	45.2

combustion reaction, leading to exergy destruction of 10.0%. Besides, the exhaust gas from the afterburner drives the turbine to produce 8.8 kW of electric power, and 9.6% exergy is destroyed. The exhaust gas from the turbine then enters the heat exchanger, which is used to preheat the air, and 1.1% exergy is destroyed. Furthermore, the remaining exhaust gas from the HX-01 drives the ARS to produce 1.1 kW of cooling. Finally, the

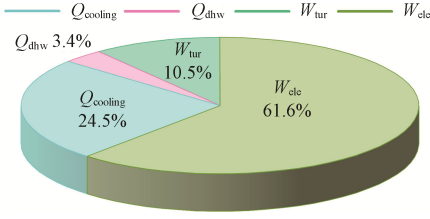


Fig. 3 A pie chart of the CCHP system outputs energy

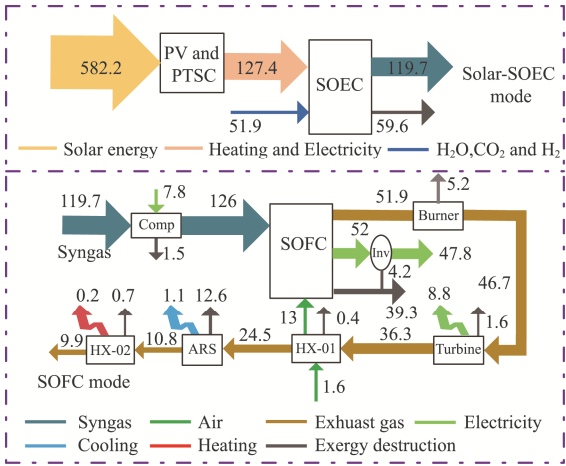
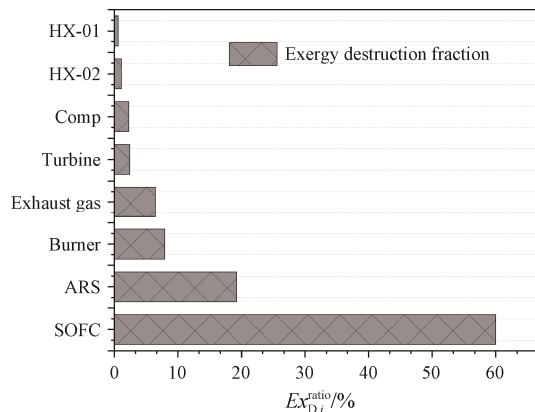


Fig. 4 Sankey diagrams of two modes in the CCHP system (kW)

Table 8 The thermodynamic properties of streams in the proposed system

Stream	$T/^\circ\text{C}$	P/kPa	$m/\text{kg}\cdot\text{h}^{-1}$	$h/\text{kJ}\cdot\text{kg}^{-1}$	$s/\text{kJ}\cdot(\text{kg}\cdot\text{K})^{-1}$	Ex/kW
1	25	101.325	72.64	-11 980.62	-3.97	27.54
2	329	101.325	72.64	-10 407.85	0.30	37.74
3	800	101.325	72.64	-9550.77	1.35	44.83
4	800	101.325	19.44	789.42	1.28	2.88
5	800	101.325	53.20	-7423.28	3.03	119.85
6	800	101.325	53.20	-7432.22	3.02	119.74
7	998.38	202.65	53.20	-6990.22	3.08	126.04
8	700	202.65	115.40	722.24	1.20	13.26
9	800	101.325	73.68	-9632.43	1.27	40.91
10	800	101.325	94.92	847.89	1.45	11.83
11	799.96	101.325	168.60	-3732.09	1.59	52.74
12	1040.71	202.65	168.60	-3732.09	1.74	46.71
13	902	101.325	168.60	-3941.28	1.78	36.28
14	592.75	101.325	168.60	-4386.36	1.13	24.54
15	170	101.325	168.60	-4938.78	0.26	10.81
16	120	101.325	168.60	-4999.83	0.12	9.99
21	25	101.325	67.20	-5469.47	-2.14	0.93
22	60	101.325	67.20	-4878.32	-1.93	1.11

**Fig. 5** The exergy loss percentage of each component in the CCHP system

residual heating is used by the HX-02 to generate 0.2 kW of domestic hot water and 6.5% of exhaust gas, and the remaining waste gas is emitted into the atmosphere.

Fig. 5 shows the exergy destruction percentages of all devices in the CCHP system. The irreversibility of electrochemical reaction makes the exergy destruction of SOFC reach 60%, and SOFC is the component having the largest exergy destruction. It is followed by ARS and afterburner, accounting for 19.2% and 7.9% of total exergy loss, respectively, which is because of the irreversible property of combustion reactions and the large temperatures difference between components and streams, respectively. The exergy destructions of the turbine, compressor, HX-02, and HX-01 account for

2.4%, 2.3%, 1.1%, and 0.6% of the total exergy destruction. The large temperature difference between the reactor and the input gas resulted in some exergy loss in these processes. In addition, the exergy destruction of the HX is usually less in the system, confirming that the temperature matching in the system is reasonable. Overall, the total exergy loss of the CCHP system is 54.8%, and the irreversibility of chemical and electrochemical reactions is the main factor causing the exergy destruction of the system. Therefore, the performance of the proposed system could be improved by optimizing reaction conditions (such as optimal operating temperature and operating pressure).

4.3 Effects of key parameters

4.3.1 The compositions of syngas

The effect of the SOEC import concentration on syngas is analyzed in Fig. 6, where the H_2/CO ratio ($M_{\text{H}_2/\text{CO}}$) is regarded as three different tests as R_U function. As the R_U was increased from 0.1 to 0.5, the $M_{\text{H}_2/\text{CO}}$ of the three tests fluctuated slowly at 4.3, 2.5 and 1.6, respectively. $M_{\text{H}_2/\text{CO}}$ reached the maximum when the ratio of H_2O and CO_2 ($M_{\text{H}_2\text{O}/\text{CO}_2}$) was 3.5; this was because an increase in the mole amount of H_2O promoted the reverse reaction of RWGS, which in turn led to an increase in the mole amount of H_2 . The above results indicated that the ratio results were consistent

with the inlet composition, which showed a rise of $M_{\text{H}_2\text{O}/\text{CO}_2}$ also generated an increase in $M_{\text{H}_2/\text{CO}}$ in the products. However, the five-fold change of R_U had a slight effect on $M_{\text{H}_2/\text{CO}}$, which suggested that only the imported gases can determine the syngas composition.

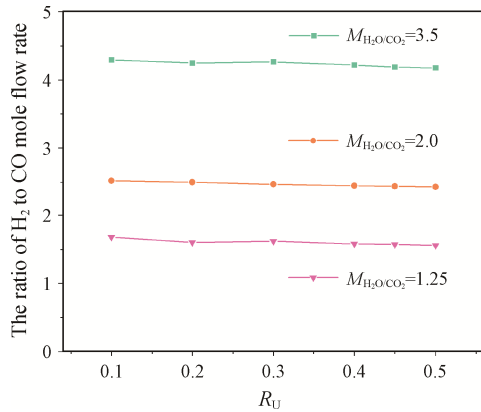


Fig. 6 The H_2/CO ratio as a function of R_U

4.3.2 Impacts of main parameters

Fig. 7 describes the impacts of the $R_{U,\text{fuel}}$ of SOFC on system performances. The electrical output from SOFC rose by 27.9% (from 42.3 kW to 54.1 kW), the cooling output and the electrical output from turbine were decreased, however, by 54.0% (decreased from 36.1 kW to 16.6 kW) and 23.1% (decreased from 10.8 kW to 8.3 kW), respectively when the $R_{U,\text{fuel}}$ was increased from 0.65 to 0.9. Besides, the exergy efficiency and the electrical efficiency rose by 17.2% (from 39.5% to 46.3%), and 17.3% (from 44.9% to 52.7%), respectively, but the energy efficiency was reduced by 11.1% (decreased from 77.8% to 69.2%) as $R_{U,\text{fuel}}$ changed. There are two main reasons for these effects: firstly, it can be seen from Eq. (31) that J_{SOFC} increased with the increase of $R_{U,\text{fuel}}$; the voltage, however, decreased only slightly due to a rise in the polarization losses at the anode, which led to higher power generation. Secondly, the increase of $R_{U,\text{fuel}}$ meant that more H_2 could be used for the electrochemical reaction of SOFC.

On the contrary, the amount of unused fuel entering the burner was reduced, which led to less exergy destruction because of its combustion. At the same time, there had less exhaust gas to drive turbines and ARS. Last but not least, the system's overall performance was degraded because the reduction in chilled water was greater than the increase in electrical power.

The influences of the mole ratio of H_2O to CO_2 ($M_{\text{H}_2\text{O}/\text{CO}_2}$) on the system energy performances are illustrated in Fig. 8(a). When an increase in $M_{\text{H}_2\text{O}/\text{CO}_2}$ was from 0.28 to 3.5, the domestic hot water output and electrical output of SOFC had no significant impact.

However, the cooling output decreased by 14.5% (reduced from 23.4 kW to 20.0 kW). The reasons for these results were that the mole fraction rate of H_2 in syngas was increased with the increase of $M_{\text{H}_2\text{O}/\text{CO}_2}$ while the mole fraction rate of CO was decreased and the WGS reaction converted CO and H_2O into H_2 and CO_2 , which led to a constant equivalent H_2 molar flow rate and

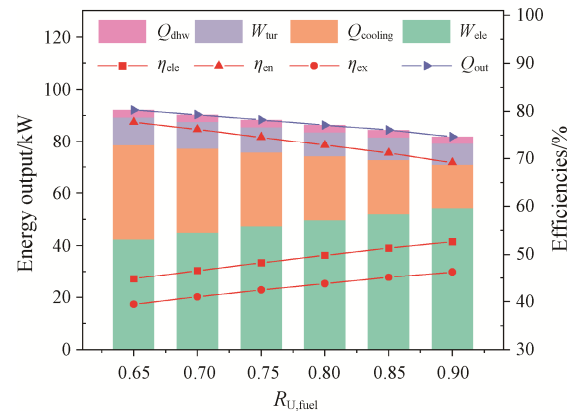
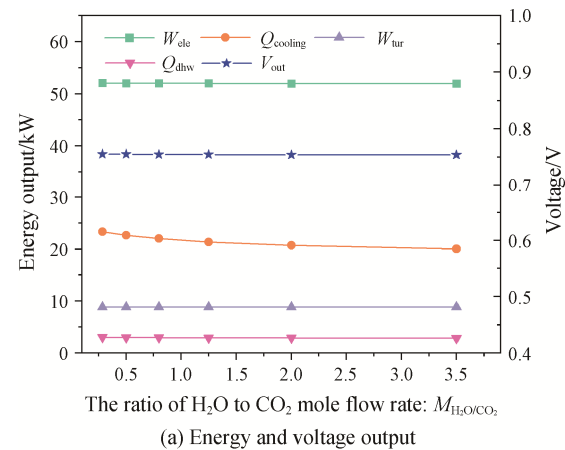
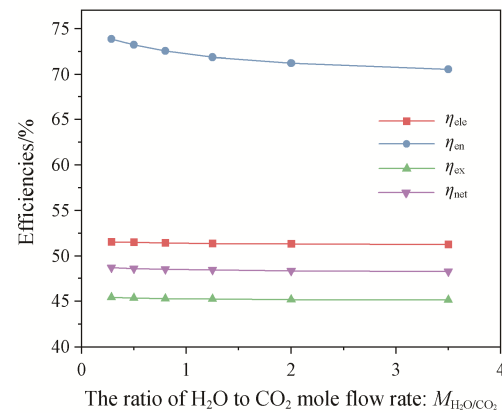


Fig. 7 The impact of $R_{U,\text{fuel}}$ on system performance



(a) Energy and voltage output



(b) Energy performances

Fig. 8 Impacts of the mole ratio of H_2O to CO_2 ($M_{\text{H}_2\text{O}/\text{CO}_2}$) on system outputs and performances

in turn caused the voltage to remain stable. Furthermore, the reason why the electricity output from the turbine did not change significantly was that the mass flow and pressure of the streams did not change significantly. Finally, as the enthalpy of H_2 was lower than that of CO , the increase of H_2 reduced the heat released from the burner, which drove the ARS to produce less cooling output.

The system performance changes with the mole ratio of H_2O to CO_2 are shown in Fig. 8(b). The electrical, exergy, and net electrical efficiencies slightly changed as the M_{H_2O/CO_2} increased from 0.28 to 3.5. Still, the increase of M_{H_2O/CO_2} decreased by 4.5% (reduced from 73.9% to 70.6%). The main reason was that the syngas energy into SOFC did not change significantly with the increase of M_{H_2O/CO_2} and the cold output decreased relatively much, which resulted in a decrease in the energy efficiency of the CCHP system.

Fig. 9 illustrates the influences of the inlet flow rate of the SOEC (M_{inlet}) on the system energy performance. When the increase in M_{inlet} was from 2.0 kmol/h to 4.5 kmol/h, the electrical output, domestic hot water, and cooling output rose by 33.1 kW, 2.3 kW, and 21.1 kW, respectively, which led to a rise in the total energy output (Q_{out}) observably, by 100.7% (from 58.6 kW to 117.6 kW). The increase of M_{inlet} meant that more H_2 was involved in the electrochemical reaction of SOFC. The quantity of unused fuel entering the burner was increased because the $R_{U,fuel}$ stayed the same, which generated more exhaust gas to drive turbines and ARS. The electrical, exergy and energy efficiency were reduced by 13.9% (decreased from 54.0% to 46.5%), 11.7% (decreased from 46.2% to 40.8%) and 10.8% (decreased from 74.2% to 66.2%), respectively. The reason for these effects was that the ohmic overpotential (η_{ohmic}), the current, and the low heat value (LHV) of the syngas entering the SOFC increased with the increasing M_{inlet} . But the increase of the LHV of syngas was larger than the decline of power, resulting that the total performance of the hybrid system was decreased.

The relationships between the energy outputs and the SOFC operating temperature (T_{SOFC}) are illustrated in Fig. 10(a). As the T_{SOFC} was increased from 800°C to 1050°C, the voltage and the electric power output were increased by 8.0% (from 0.75 V to 0.81 V) and 7.3% (from 52.0 kW to 55.8 kW), respectively. The activation and the concentration overpotentials increased with increasing temperature. Still, the ohmic overpotential significantly reduced with it. Eq. (30) shows that a decrease in overpotential caused an increase in voltage, increasing electrical power. Besides, raising T_{SOFC} the fuel cell outlet temperature could drive the turbine and ARS to produce more electrical and cooling output.

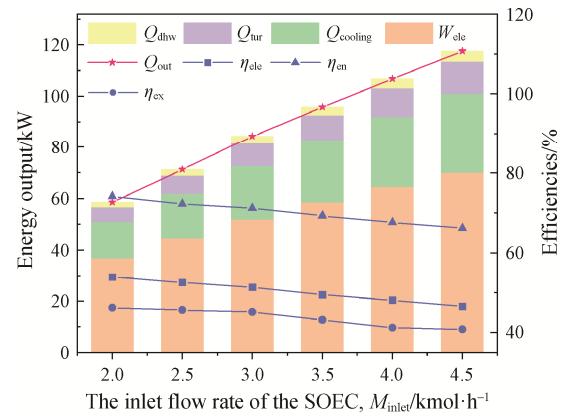
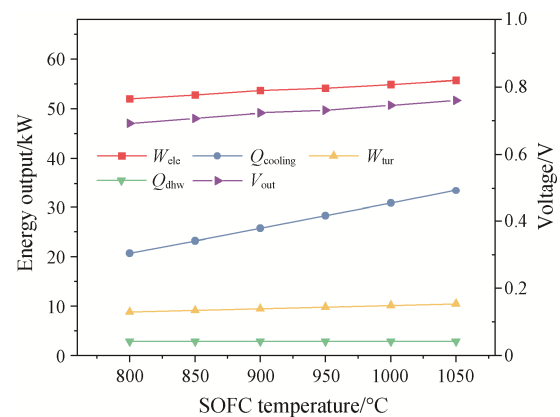
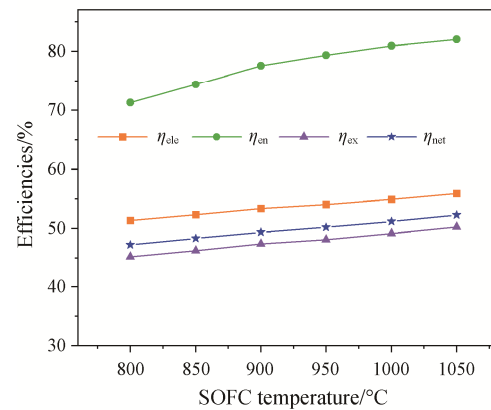


Fig. 9 The impacts of M_{inlet} change on system performances



(a) Outputs of power, cooling, domestic hot water and voltage



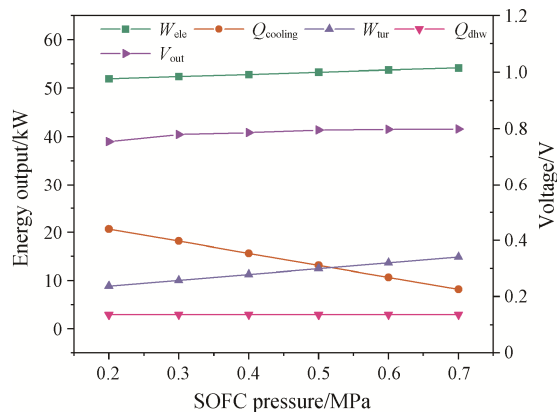
(b) System performances

Fig. 10 Impacts of the T_{SOFC} on system energy outputs and performances

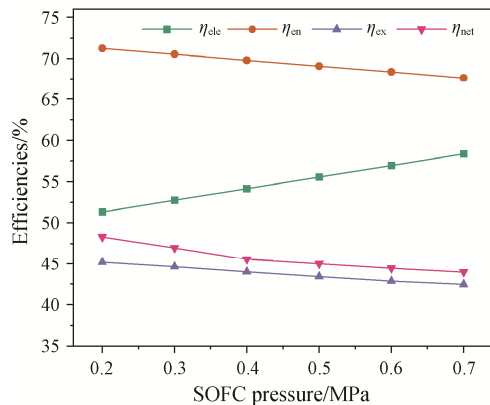
Fig. 10(b) demonstrates the relationships between energy performances and T_{SOFC} . The exergy and energy efficiency increased by 11.3% (from 45.2% to 50.3%) and 12.3% (from 71.3% to 80.1%), respectively, when an increase in T_{SOFC} from 800°C to 1050°C. The main reason for the improved performance was the more active electron transfer in the electrolyte. At the same time, the increase in exhaust gas temperature allows more waste

heat to be utilized, which further improves the system performance.

The relationships between energy outputs and the voltage and the SOFC pressure (p_{SOFC}) are illustrated in Fig. 11(a). As the p_{SOFC} was increased from 0.2 MPa to 0.7 MPa, the power output of the turbine and the electric power output of SOFC were increased by 69.3% (from 8.8 kW to 14.9 kW) and 4.2% (from 52 kW to 54.2 kW), respectively; besides, the voltage was increased by 6.7% (from 0.75 V to 0.80 V). However, the cooling output was negatively correlated with the increase of p_{SOFC} and reduced by 60.9% (decreased from 20.7 kW to 8.1 kW). This was because the overpotential on the V_{SOFC} decreased as the p_{SOFC} increased, which led to both voltage and electrical power increase. In addition, the rise in the turbine's power output was due to the rise in inlet pressure, which led to a reduction in the flow of exhaust gas entering the ARS and a reduction in the cooling output.



(a) Outputs of power, cooling, heating and voltage



(b) System performances

Fig. 11 Impacts of the p_{SOFC} on system energy outputs and performances.

Fig. 11(b) demonstrates the relationship between the energy performances and the p_{SOFC} . As the p_{SOFC} was increased from 0.2 MPa to 0.7 MPa, the energy, net electrical and exergy efficiencies were reduced by 5.2%

(decreased from 71.3% to 67.6%), 8.9% (decreased from 48.3% to 44.0%) and 6.0% (decreased from 45.2% to 42.5%), respectively. The compressor's energy consumption increased with the increase of pressure, which led to efficiency reduction. On the contrary, the increase of p_{SOFC} increased the electrical efficiency of SOFC by 13.8% (from 51.3% to 58.4%). This was because the increase of pressure had a positive on improving the rate of mass transfer of the reactant, promoting the electrochemical reaction of SOFC, and increasing the electrical power. Furthermore, the electrical efficiency increased linearly. To sum up, both the operating pressure and temperature of the SOFC played indispensable roles in the CCHP system's performance.

5. Conclusions

A novel CCHP system integrated with solar-assisted SOEC and SOFC had been simulated and analyzed. The model had been conducted by considering the solar energy in thermal and PV combined with the SOEC to produce the syngas at higher solar radiation time and generate the electrical power, heat energy, and cooling energy by utilizing the storage syngas in SOFC mode. Through the thermodynamics evaluation, the major conclusions were:

(1) The SOFC mode provides higher net electrical and overall energy efficiency. Although the efficiency of syngas production is high, solar radiation as system input energy and the low efficiency of solar modules lead to the decline of the overall system efficiency.

(2) Under the design condition, the irreversibility of electrochemical reaction makes the exergy destruction of SOFC reach 60%, which makes SOFC the largest component of the exergy destruction.

(3) The proposed system's energy and exergy efficiencies are 19.0% and 20.5% in solar-assisted SOEC mode, 71.3% and 45.2% in SOFC mode, respectively. The energy efficiency of the SOFC is reduced by 12.4% (decreased from 77.8% to 69.2%) when the fuel conversion rate of SOFC is increased from 0.65 to 0.9. In comparison, the electrical and exergy efficiencies rise by 17.3% (from 44.9% to 52.7%) and 17.2% (from 39.5% to 46.3%), respectively.

(4) The output power of SOFC is the key factor to determine the proposed system's performance. Furthermore, the operating pressure and temperature of the SOFC play a significant role in the output power. The electrical efficiency increased by 9.0% (from 51.3% to 55.9%); the exergy and energy efficiency increased by 11.3% (from 45.2% to 50.3%) and 12.3% (from 71.3% to 80.1%), respectively, when an increase in the temperature of SOFC from 800°C to 1050°C. As the pressure of

SOFC is increased from 0.2 MPa to 0.7 MPa, the energy, net electrical and exergy efficiencies is reduced by 5.1%, 7.1% and 6.0%, respectively. Still, the increase of the pressure of SOFC increases the electrical efficiency by 13.6%.

(5) In this study, the thermodynamic performances were discussed. The construction and operation of the proposed system must be cost-effective. Future work is needed to present the economic and environmental analysis to discuss its feasibility; also the optimal system configurations and operation strategy are studied.

Acknowledgments

This research has been supported by the National Natural Science Foundation of China (Grant No. 51876064 and 52090064) and the Bureau of Shihezi Science & Technology (Grant No. 2021ZD02).

References

- [1] Akikur R.K., Saidur R., Ping H.W., Ullah K.R., Comparative study of stand-alone and hybrid solar energy systems suitable for off-grid rural electrification: A review. *Renewable and Sustainable Energy Reviews*, 2013, 27: 738–752.
- [2] Wang J., Han Z., Guan Z., Hybrid solar-assisted combined cooling, heating, and power systems: A review. *Renewable and Sustainable Energy Reviews*, 2020, 133: 110256.
- [3] Ullah K.R., Saidur R., Ping H.W., Akikur R.K., Shuvo N.H., A review of solar thermal refrigeration and cooling methods. *Renewable and Sustainable Energy Reviews*, 2013, 24: 499–513.
- [4] Wang Y., Leung D.Y.C., Xuan J., Wang H., A review on unitized regenerative fuel cell technologies, part B: Unitized regenerative alkaline fuel cell, solid oxide fuel cell, and microfluidic fuel cell. *Renewable and Sustainable Energy Reviews*, 2017, 75: 775–795.
- [5] Gómez S.Y., Hotza D., Current developments in reversible solid oxide fuel cells. *Renewable and Sustainable Energy Reviews*, 2016, 61: 155–174.
- [6] Ferrero D., Lanzini A., Leone P., Santarelli M., Reversible operation of solid oxide cells under electrolysis and fuel cell modes: Experimental study and model validation. *Chemical Engineering Journal*, 2015, 274: 143–155.
- [7] Redissi Y., Bouallou C., Valorization of carbon dioxide by co-electrolysis of CO₂/H₂O at high temperature for syngas production. *Energy Procedia*, 2013, 37: 6667–6678.
- [8] Ebbesen S.D., Graves C., Mogensen M., Production of synthetic fuels by co-electrolysis of steam and carbon dioxide. *International Journal of Green Energy*, 2009, 6(6): 646–660.
- [9] Cinti G., Baldinelli A., Di Michele A., Desideri U., Integration of solid oxide electrolyzer and fischer-tropsch: a sustainable pathway for synthetic fuel. *Applied Energy*, 2016, 162: 308–320.
- [10] Schiffer Z.J., Manthiram K., Electrification and decarbonization of the chemical industry. *Joule*, 2017, 1(1): 10–14.
- [11] Wang F., Wang L., Ou Y., Lei X., Yuan J., Liu X., Thermodynamic analysis of solid oxide electrolyzer integration with engine waste heat recovery for hydrogen production. *Case Studies in Thermal Engineering*, 2021, 27: 101240.
- [12] Akikur R.K., Saidur R., Ping H.W., Ullah K.R., Performance analysis of a co-generation system using solar energy and SOFC technology. *Energy Conversion and Management*, 2014, 79: 415–430.
- [13] Becker W.L., Braun R.J., Penev M., Melaina M., Production of Fischer-Tropsch liquid fuels from high temperature solid oxide co-electrolysis units. *Energy*, 2012, 47(1): 99–115.
- [14] Qi H., Zhang J., Tu B., Yin Y., Zhang T., Liu D., Extreme management strategy and thermodynamic analysis of high temperature H₂O/CO₂ co-electrolysis for energy conversion. *Renewable Energy*, 2022, 183: 229–241.
- [15] Mottaghizadeh P., Santhanam S., Heddrich M.P., Friedrich K.A., Rinaldi F., Process modeling of a reversible solid oxide cell (r-SOC) energy storage system utilizing commercially available SOC reactor. *Energy Conversion and Management*, 2017, 142: 477–493.
- [16] Weimer T., CO₂ removal and fixation solar high temperature syngas generation for fuel synthesis. *Energy Conversion and Management*, 1997, 38: S379–S384.
- [17] Xi C., Sang J., Wu A., Yang J., Qi X., Guan W., Electrochemical performance and durability of flat-tube solid oxide electrolysis cells for H₂O/CO₂ co-electrolysis. *International Journal of Hydrogen Energy*, 2022, 47(18): 10166–10174.
- [18] Stoots C.M., O'Brien J.E., Herring J.S., Hartvigsen J.J., Syngas production via high-temperature coelectrolysis of steam and carbon dioxide. *Journal of Fuel Cell Science and Technology*, 2009, 6(1): 011014.
- [19] Stoots C., O'Brien J., Hartvigsen J., Results of recent high temperature coelectrolysis studies at the Idaho National Laboratory. *International Journal of Hydrogen Energy*, 2009, 34(9): 4208–4215.
- [20] J. Meusinger E.R., U. Stimming., Reforming of natural gas in solid oxide fuel cell systems. *Journal of Power Sources*, 1998, 71: 315–320.
- [21] Williams M.C., Strakey J.P., Singhal S.C., U.S. distributed generation fuel cell program. *Journal of Power Sources*, 2004, 131(1–2): 79–85.

- [22] Bauen A., Fuel cells for distributed generation in developing countries—an analysis. *International Journal of Hydrogen Energy*, 2003, 28(7): 695–701.
- [23] Jens Palsson A.S., Lars Sjunnesson., Combined solid oxide fuel cell and gas turbine systems for efficient power and heat generation. *Journal of Power Sources*, 1999, 86: 442–448.
- [24] Tian M., Yu Z., Zhao H., Yin J., Thermodynamic analysis of an integrated solid oxide fuel cell, Organic Rankine Cycle and absorption chiller trigeneration system with CO₂ capture. *Energy Conversion and Management*, 2018, 171: 350–360.
- [25] Al-Sulaiman F.A., Hamdullahpur F., Dincer I., Performance assessment of a novel system using parabolic trough solar collectors for combined cooling, heating, and power production. *Renewable Energy*, 2012, 48: 161–172.
- [26] AlZahrani A.A., Dincer I., Thermodynamic and electrochemical analyses of a solid oxide electrolyzer for hydrogen production. *International Journal of Hydrogen Energy*, 2017, 42(33): 21404–21413.
- [27] Cinti G., Discepoli G., Bidini G., Lanzini A., Santarelli M., Co-electrolysis of water and CO₂ in a solid oxide electrolyzer (SOE) stack. *International Journal of Energy Research*, 2016, 40(2): 207–215.
- [28] Chan S., Xia Z., Polarization effects in electrolyte electrode supported solid oxide fuel cell. *Journal of Applied Electrochemistry*, 2002, 32: 339–347.
- [29] Tanim T., Bayless D.J., Tremblay J.P., Modeling of a 5 kWe tubular solid oxide fuel cell based system operating on desulfurized JP-8 fuel for auxiliary and mobile power applications. *Journal of Power Sources*, 2013, 221: 387–396.
- [30] Wang J., Yang Y., Energy, exergy and environmental analysis of a hybrid combined cooling heating and power system utilizing biomass and solar energy. *Energy Conversion and Management*, 2016, 124: 566–577.
- [31] Yan R., Wang J., Cheng Y., Ma C., Yu T., Thermodynamic analysis of fuel cell combined cooling heating and power system integrated with solar reforming of natural gas. *Solar Energy*, 2020, 206: 396–412.
- [32] Doherty W., Reynolds A., Kennedy D., Computer simulation of a biomass gasification-solid oxide fuel cell power system using Aspen Plus. *Energy*, 2010, 35(12): 4545–4555.
- [33] Zhang W., Croiset E., Douglas P.L., Fowler M.W., Entchev E., Simulation of a tubular solid oxide fuel cell stack using AspenPlus™ unit operation models. *Energy Conversion and Management*, 2005, 46(2): 181–196.
- [34] Somers C., Simulation of absorption cycles for integration into refining processes. 2009, <http://hdl.handle.net/1903/9394>.